Open Ceramics 25 (2026) 100884

Contents lists available at ScienceDirect

Open Ceramics

journal homepage: www.sciencedirect.com/journal/open-ceramics

# Magnetic alkali-activated foams from soda-lime glass and volcanic ash enabling efficient synergistic dye removal

Francesco Lanero [#], Giulia Tameni [#], Eleonora Russo, Paolo Sgarbossa, Enrico Bernardo [*]

*Department of Industrial Engineering, University of Padova, Padova, Italy*

ARTICLE INFO

*Keywords:*
Adsorption
Alkali activation
Magnetic foams
Photocatalysis
Soda-lime glass
Volcanic ash

ABSTRACT

As a solution to clean water scarcity, it is essential to develop new inexpensive and eco-friendly materials for wastewater treatment, since conventional methods are often energy-intensive, dependent on non-renewable and, in general, unsuitable for large-scale and sustainable applications. In this work, the preparation of magnetic foams via mild alkali activation (KOH, 3 M) process for water purification is reported. The process uses Mt. Etna volcanic ash and unemployed fraction of soda-lime glass obtained from purification of glass containers. Magnetic properties were imparted by the introduction of silica-coated magnetite nanoparticles at 5 % (m/m) and 10 % (m/m). The large surface area of the resulting foams makes them highly promising as adsorbent for dye removal. Additionally, the natural presence of $TiO_2$ and $Fe_2O_3$ in the volcanic ash contributes to photocatalytic activity. Both adsorption and photocatalytic performance were evaluated using methylene blue aqueous solution (10 mg/L) as model dye. An increased removal efficiency was observed following the incorporation of magnetite nanoparticles, reaching up to 96 %. These results highlight the potential of converting industrial and natural waste into functional materials for sustainable wastewater treatment applications.

## 1. Introduction

The scarcity of water remains a global challenge, substantially constraining progress towards comprehensive sustainability. This issue is further intensified by the contamination of water resources with industrial pollutants. Additionally, synthetic dyes - extensively utilized in the textile, cosmetic, and printing industries - are frequently released into the water through industrial wastewater [1]. The release of such waste contributes to environmental degradation, and also poses considerable public health risks.

To contrast pollution, industries are increasingly implementing various wastewater treatment strategies aimed at effectively removing pollutants and ensuring compliance with environmental standards [2,3]. Although numerous techniques have been developed for the treatment of water containing dyes and heavy metals [4,5], the current approaches often face limitations related to high operational costs, complexity, and reduced efficiency at variable contaminants concentration. Chemical methods, in particular, produce undesirable by-products and residues that can persist in the environment and need to be treated to prevent contamination. At the same time, biological techniques face certain limitations, especially regarding the complete removal of colour dyes [6].

In such context, adsorption technologies are recognized as very promising, due to their simplicity, low operational costs, potential for high effectiveness, and applicability to a wide range of pollutants [7–10]. In this context, the present investigation is dedicated to the synthesis of a new adsorbent material for dye removal, combining magnetism and photocatalytic properties. The same is intended as an alternative to current adsorbent materials including polymer, carbon-based materials, clay-based materials, metal-organic framework (MOFs) materials, and biosorbents [11].

Besides these classes of materials, porous alkali activated materials (AAMs) emerge as viable solutions for water and wastewater management and dye removal [12]. Alkali-activated materials are typically produced by the reaction of alumino-silicate precursor powders suspended in concentrated alkaline solutions [13]; in the subclass of geopolymers, 'oligomers' released after the dissolution of alumino-silicate are found to recombine into three-dimensional network structures, corresponding to hydrated alkali alumino-silicate 'zeolite-like' gels [14].

Recent findings on AAMs based exclusively on fine glass powders,

* Corresponding author.
*E-mail address:* enrico.bernardo@unipd.it (E. Bernardo).
[#] These authors contributed equally to the manuscript

https://doi.org/10.1016/j.oceram.2025.100884
Received 10 September 2025; Received in revised form 6 November 2025; Accepted 14 November 2025
Available online 19 November 2025

however, have suggested a new 'cold-consolidation' mechanism, with advantages in overall sustainability. In fact, glass powders undergo attack from a relatively diluted alkali hydroxide solution (< 3 M) [15,16], and convert into stable blocks just after drying. The mutual adhesion of glass particles is realized by condensation reactions at the contact points, involving Si-OH, Al-OH and B-OH surface groups (resulting from the same alkaline attack). Condensation reactions recreate strong bonds (Si-O-Si, Al-O-Si, B-O-Si), supporting 'skeletons' of glass particles, filled by the secondary phases, consisting of gels exhibiting varying degree of solubility [17], from reactions involving glass components released in solution, and crystalline phases (i.e., alkali carbonates). Foams may be easily formed by gas release at the early stages of consolidation, operated by perborates and helped by slight additions of surfactants [18,19].

To minimize the use of virgin materials, and implement the upcycling strategies, soda-lime glass waste fraction (deriving from the purification of cullet of container glass) [20] and volcanic ash from natural eruptions [21] may be coupled for more complex AAMs from mild activation and foaming [22]. The hardening mechanism, in this specific case, suggests that the chemical species (silicates, aluminates, etc.) released into the solution, do not solely contribute to the gel phase, but also promotes the growing of natural zeolites, which enhance the adsorption capability of cold-consolidated foams. The porous nature enhances dyes removal efficiency by offering active adsorption sites, and the interconnected pore system enables efficient diffusion of dyes molecules into the alkali activated foams [23,24]. Moreover, considering the presence of $Fe_2O_3$ and $TiO_2$ in volcanic ash utilized within alkali-activated foams, these oxides may function as effective photocatalytic supports, leading to a double adsorption/photocatalytic effect in the dye removal [25–27].

Considering the application in a real wastewater purification system, sorbents should be refined also in the operational aspects. In this context, the use of magnetic materials is gaining increasing attention due, above all, to the possibility of being easily recovered from treated water using magnets, thus avoiding the need for filtration or centrifugation, which are more complex and costly operations. One of the most common and easiest approaches to create magnetic three dimensional manufacts is the introduction of magnetite nanoparticles [28–30].

The present work offers a new prospective for glass/volcanic ash alkali activated foams. In fact, despite the use of such materials in construction and building application as thermal and sound insulator [31], dye removal via synergistic adsorption–photocatalytic effect is a not yet investigated application. Herein we reported our efforts to combine the advantages related to the combination of AAMs, volcanic ash and magnetic nanoparticles, such as the use of recycled glass materials, low cost of the volcanic ash, large surface area of the foam, to obtain magnetic adsorbent foamed samples with enhanced photocatalytic behaviour which can serve as low-temperature-prepared alternatives to the more common adsorbent materials like carbon-based adsorbents, typically synthesized at very high temperatures [32]. Magnetite nanoparticles were synthesized by coprecipitation and subsequently functionalized with a silica layer in order to improve the adhesion with the raw materials during the alkali activation mechanism by siloxane bonds and introduced during the foamed samples preparation [33,34]. The morphology and the structure of the nanoparticles and then of the foams were characterized and their adsorption and photocatalytic behaviour under visible light investigated using methylene blue as dye model due to its low cost, availability and easy determination.

## 2. Materials and methods

### 2.1. Raw materials

The preparation of alkali activated foams employed the soda-lime glass (SLG) waste together with volcanic ash (VA). Soda-lime glass was kindly provided by SASIL S.r.l (Brusnengo, Biella, Italy) in the form of fine powders with a particle size of less than 32 μm [15]. The volcanic ash (VA) consisted of municipal waste collected from public spaces following the explosive eruptions of Mount Etna in 2021. Volcanic ash powder was obtained by dry milling (Pulverisette 6, Fritsch GmbH, Idar-Oberstein, Germany) and sieved below 75 μm, instead soda-lime glass powder was used as-received.

Table 1 provided the chemical composition of the two fundamental raw materials, as determined through X-ray fluorescence analysis (Bruker S8 TIGER, Bruker AXS, Germany) [22].

Soda-lime glass-to-volcanic ash ratio was fixed as 1 for all the formulations. The alkali activated solution was potassium hydroxide solution (KOH, 3 M) prepared by dissolving KOH pellets (reagent grade, Sigma-Aldrich, Gillingham, UK) into distilled water.

Iron(II) chloride $FeCl_2{\cdot}4H_2O$ (≥ 99 %), Iron (III) $FeCl_3{\cdot}6H_2O$ (≥ 99 %), Tetraethyl orthosilicate (TEOS) (98 %) and Ammonium hydroxide $NH_4OH$ (25 % m/V) were purchased from Sigma-Aldrich and used as received.

### 2.2. Methods

#### 2.2.1. Magnetic nanoparticles MNP-$Fe_3O_4$

Magnetic nanoparticles, referred as MNP-$Fe_3O_4$, were prepared via a simple coprecipitation method [33]. Briefly, $FeCl_2{\cdot}4H_2O$ (1.03 g, 8.13 mmol) and $FeCl_3{\cdot}6H_2O$ (2.78 g, 10.28 mmol) were magnetically stirred in 100 mL of deionized water under a $N_2$ atmosphere until complete dissolution. Then, $NH_4OH$ 25 % w/v (12 mL, 85.59 mmol) was added under vigorous stirring to rapidly increase the pH to 11, leading to the precipitation of MNPs-$Fe_3O_4$. The mixture was stirred at room temperature for 1 h. Subsequently, the system was allowed to decant, and the product was washed three times with deionized water and twice with ethanol. Finally, the product was dried under vacuum ($10^{-2}$ mbar) for 24 h.

In order to cover the nanoparticles surface, the as-prepared MNPs-$Fe_3O_4$ (900 mg, 3.89 mmol) were dispersed under vigorous stirring in a mixture of deionized water and EtOH (1:4, 450 mL) along with $NH_4OH$ 25 % w/v (2.1 mL, 14.98 mmol). Tetraethyl orthosilicate (TEOS) (2.5 mL, 11.20 mmol) was then added dropwise, and the system was stirred at room temperature overnight. Afterward, the resulting $Fe_3O_4$@$SiO_2$ was separated by centrifugation, washed twice with water, once with ethanol, and finally dried under vacuum ($10^{-2}$ mbar) for 24 h [34].

#### 2.2.2. Sample preparation

Alkali activated foams were prepared by initially mixing glass powder (5.0 g) and volcanic ash (5.0 g) in the alkaline solution, with a liquid-to-solid ratio of 0.5. The slurries were stirred for two hours at rotation speed of 500 rpm and at the end of two hours, sodium perborate monohydrated (SPM, $NaBO_3H_2O$, ≥ 99 %, Sigma-Aldrich, Gillingham, UK and sodium dodecyl sulfated (SDS, $CH_3(CH_2)_{11}OSO_3Na$, ≥ 99 %, Sigma-Aldrich, Gillingham, UK) were added at a concentration of 1 wt percent (wt %) related to the mass of the powder, as foaming and stabilizing agent, respectively [18,19]. Simultaneously, $Fe_3O_4$@$SiO_2$ were incorporated at concentration of 0, 5 and 10 wt % referred to the liquid fraction. Finally, all the additives were homogenized by mixing for 5 min at 2000 rpm. The resulting slurries were casted in plastic moulds (10 mm x 10 mm x 10 mm, open moulds) and left to rest in an oven at 75 °C and demolded after three days. The obtained foams are cubic, with sides of 0.9 mm. In line with the progressive increase in the percentage of embedded nanoparticles, the samples were designed as A, B and C to facilitate clarity and precise identification, as shown in Table 2.

#### 2.2.3. Characterization

The infrared spectra were acquired by attenuated total reflectance Fourier Infrared Spectroscopy (ATR-FTIR) analyses. The spectra were recorded with a Perkin-Elmer Spectrum 100 instrument in the range of 4000 - 750 $cm^{-1}$.

The morphology and microstructure of the nanoparticles were

**Table 1**
Chemical composition of starting raw materials.
* LOI (Loss on Ignition): Mass loss after calcination at 900 °C.

| | $SiO_2$ [ % m/m] | $TiO_2$ [ % m/m] | $Al_2O_3$ [ % m/m] | $Fe_2O_3$ [ % m/m] | MgO [ % m/m] | CaO [ % m/m] | $Na_2O$ [ % m/m] | $K_2O$ [ % m/m] | $SO_3$ [ % m/m] | LOI [ %] |
|---|---|---|---|---|---|---|---|---|---|---|
| **SLG** | 71.7 | 0.1 | 0.7 | 0.1 | 3.3 | 10.1 | 13.2 | 0.1 | 0.2 | 0.5 |
| **VA** | 46.8 | 1.9 | 16.0 | 11.9 | 6.3 | 9.8 | 2.8 | 1.8 | 0.3 | 2.4 |

**Table 2**
Designed mixture of the amount of $Fe_3O_4$@$SiO_2$ in the alkali activated foams.

| Sample | $Fe_3O_4$@$SiO_2$ [% m/m] |
|---|---|
| A | 0 |
| B | 5 |
| C | 10 |

characterized by transmission electron microscopy (TEM) and high-angle annular dark-field (HAADF) scanning transmission electron microscopy (HAADF-STEM) using TEM JEOL F200 operated at 200 kV. Elemental analysis and mapping were performed using a JEOL 100 $mm^2$ silicon drift energy dispersive X-ray spectrometer (EDX). A carbon supported copper grids, 400 mesh size, were used for preparation of the sample.

The morphology and semi-quantitative elemental composition of the samples were analysed by means of scanning electron microscopy (SEM, FEI, Quanta 200 **ESEM**, Eindhoven, The Netherlands), coupled with energy dispersive spectroscopy (**EDS/EDAX** Genesis, Mahwah, NJ, USA).

X-ray diffraction measurements were performed on raw materials and alkali activated foams. To analyze the mineralogical composition of the obtained foams a Bruker D8 Advance (Karlsruhe, Germany) was used. The analysis utilizes CuKα radiation with a wavelength of 0.15418 nm, operated at a voltage of 40 kV and a current of 40 mA. The scanning range was set in a range of 2θ =10 to 70°, with a step size of 0.05° and counting duration of 2 s. Phase identification is performed using Match® software package (Crystal Impact GbR, Bonn, Germany) in conjunction with data obtained from the Powder Diffraction File (PDF)-2 database.

The volumetric mass density ($\rho_{geom}$) of the samples corresponding to each mixture was determined using the formula $\rho_{geom} = m/V$, where m and V represent the mass and the volume of the samples, respectively. The bulk density was based on measurements taken from five cubic specimens. Furthermore, both apparent ($\rho_{app}$) and true ($\rho_{true}$) density were measured by means of a helium pycnometer (Ultrapyc 3000, Anton Paar GmbH, Graz, Austria) on bulk and crushed samples. The open (OP) and closed porosities (CP) of the newly developed porous materials were calculated from the obtained density data.

#### 2.2.4. Photocatalysis test

The adsorption and photocatalytic properties of the foamed samples were evaluated using a methylene blue ($C_{16}H_{18}ClN_3S$) aqueous solution (10 mg/L) as a model organic pollutant. Adsorption tests were conducted in a beaker under magnetic stirring at 25 °C. A foamed sample (0.8–1.0 g) was immersed in 100 mL of the methylene blue solution, ensuring that it did not encounter the magnetic stir bar to preserve the structural integrity of the material. At predetermined time intervals, 3 mL aliquots were withdrawn and filtered for spectrophotometric analysis.

Two distinct experimental conditions were employed to the comprehensively assess the performance of the material. The first condition involve adsorption experiments conducted in the absence of light, aimed at evaluating the physical adsorption capacity of the material. The second condition entailed photocatalytic degradation test under visible light conditions, using a VWR VisiLight® LED3 lamp (36 W, 5700 K, 730 lm) as the light source. All experiments were performed in duplicate.

The concentration of methylene blue in the aliquots was determined using the Lambert–Beer law. UV–Vis spectra were recorded in the 200–700 nm range using a PerkinElmer LAMBDA 365+ UV–Vis spectrophotometer, with the absorbance measured at 663 nm. The schematic representation is reported in Fig. 1.

## 3. Results and discussion

### 3.1. Synthesis and characterization of $Fe_3O_4$@$SiO_2$

Magnetic nanoparticles MNP-$Fe_3O_4$ were prepared via a simple coprecipitation method [33]. To enhance their interaction with the volcanic ash powder, mainly composed of silica, a functionalization of the outer layer of magnetite nanoparticles was performed using the Stöber method [34].

The silica coating on $Fe_3O_4$ particles was initially verified by ATR-FTIR. In Figure S1, the FTIR spectrum is reported. The main silica vibrations were observed in the 1000–1250 $cm^{-1}$ range (very strong antisymmetric stretching of the Si-O-Si bond), at 960 $cm^{-1}$ (stretching of Si-OH and symmetric stretching of Si-O-Si), and at 795 $cm^{-1}$ (symmetric stretching vibration of Si-O-Si). The broad band between 3600 and 2900 $cm^{-1}$ was attributed to the O-H stretching of water adsorbed on the silanol groups of silica [35,36].

The coated nanoparticles were then characterized by ESEM-EDX, to determine the actual amount of bonded silica. In Fig. 2 the mapping analysis is shown, and the homogeneous distribution of Fe, O and Si is clearly demonstrated, proving the homogeneously success of the silanization reaction. From the elemental analysis carried out by means of

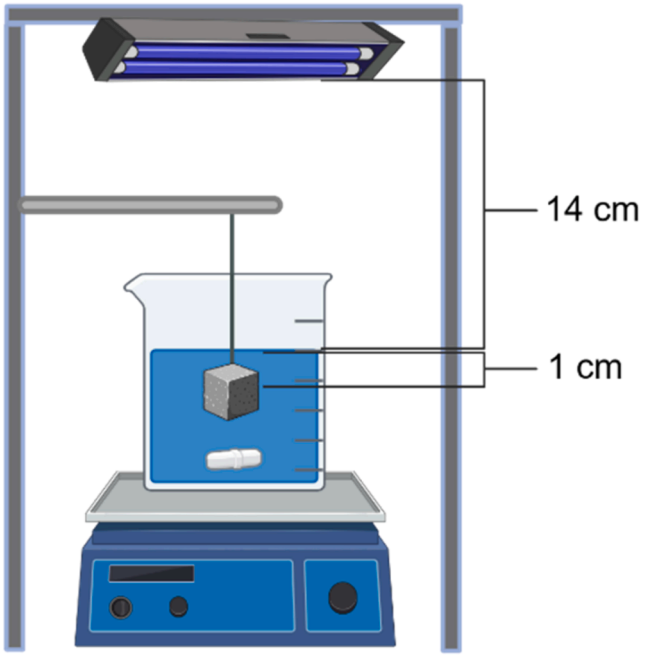


**Fig. 1.** Schematic representation of the photocatalytic test setup.

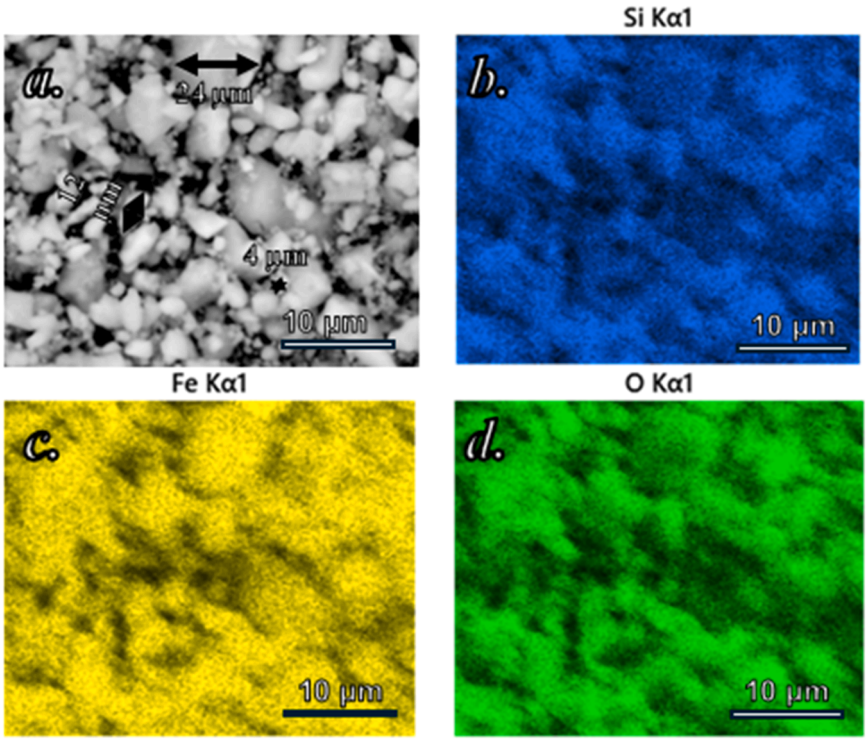


**Fig. 2.** ESEM micrographs (a) and energy dispersive X-ray (EDX) mapping analysis (b, c and d) of $Fe_3O_4$@$SiO_2$.

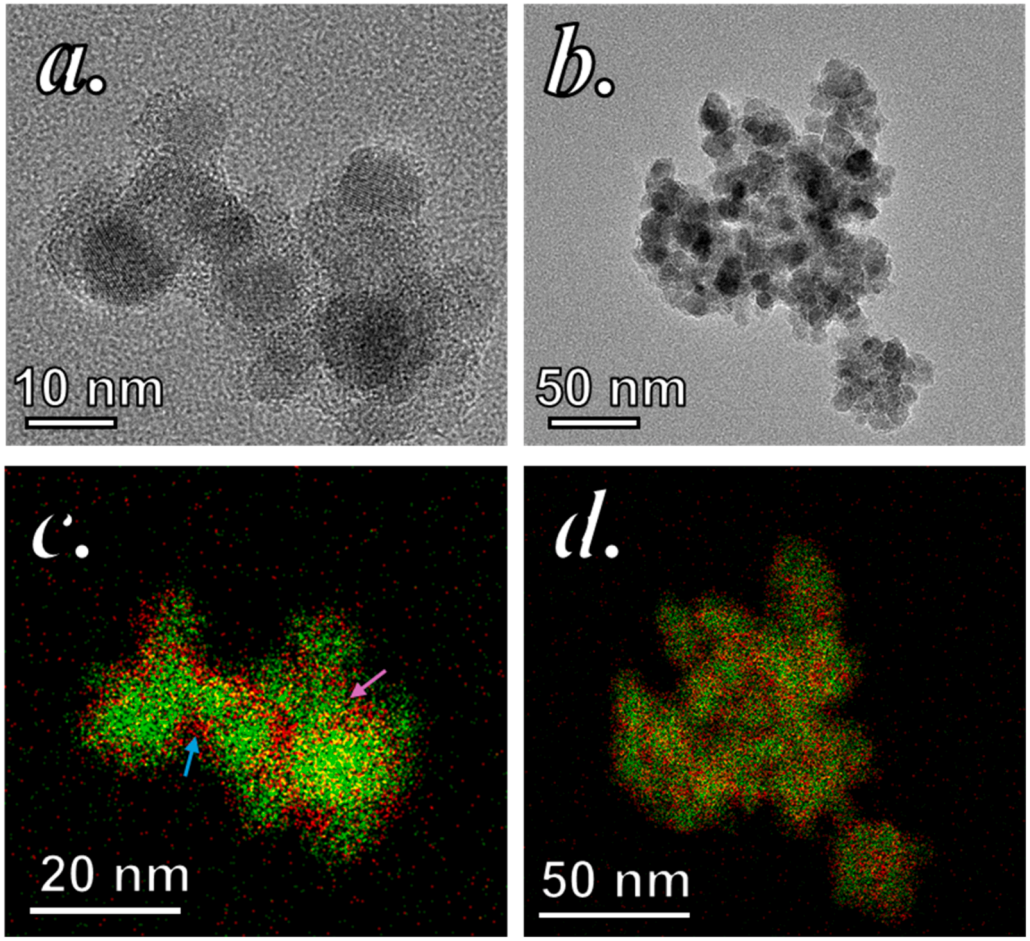


**Fig. 3.** TEM micrographs of $Fe_3O_4$@$SiO_2$ (a and b) with their correspondent elemental mapping by EDX analysis (respectively c and d). Si in red and Fe in green.

EDX, the amount of silica was calculated as the average of three measurements: 17.01 % m/m of $SiO_2$ and 82.99 % m/m of $Fe_3O_4$, showing a degree of silanization consistent with the ones reported by Teixeira de Mendonça et al. [35].

Finally, the morphology and microstructure of the nanoparticles was studied by transmission electron microscopy (TEM) and elemental mapping analysis performed by energy dispersive X-ray (EDX).

The $Fe_3O_4$@$SiO_2$ (Figs. 3 and S2) is present as aggregates with irregular shapes and sizes ranging from 50–350 nm. Their agglomeration derived by the assembly of smaller magnetite nanoparticles of 5–12 nm during the reaction with tetraethyl orthosilicate (TEOS).

As reported in literature, the aggregation is expected despite the hydrophilicity of magnetite nanoparticles, since no surfactant was used in the synthesis. In this condition the nanoparticles are easy to aggregate to reduce surface energy in the reaction media obtaining silica-coated magnetite particles with irregular morphologies [35,37].

As reported by Yang et al. [37], the use of a surfactant like trisodium citrate allows the magnetite nanoparticles to be charged on the surface, leading to stronger electrostatic repulsion which prevents their aggregation to obtain colloidal magnetic silica $Fe_3O_4$@$SiO_2$ particles with well-defined core-shell structure. In our case, the aim of the core shell functionalization is not the synthesis of perfectly covered nanoparticles, but a combination of covered regions to improve the adhesion during the foam synthesis and uncovered portions to make possible the interaction with the methylene blue during the adsorption and photocatalytic tests.

From the micrographs is possible to distinguish crystalline regions of the magnetite nanoparticles and amorphous regions of the silica coating. The distinction is clearly visible by EDX mapping of the particles (Fig. 3c-d), where the Si is represented by the red and the Fe by the green colour. The Si is not distributed homogeneously around the Fe core. In particular, some regions are completely covered (blue arrow in Fig. 3c), enhancing the adhesion during the foam synthesis, while others remain partially uncovered (pink arrow in Fig. 3c), allowing for a direct interaction of the iron core with the pollutant during the dye removal tests.

### 3.2. Synthesis and characterization of volcanic-based magnetic composites

#### 3.2.1. Mineralogical characterization

The mineralogical analysis of the raw materials and the prepared alkali activated foams was presented in Fig. 4. The soda-lime glass powder employed in the process revealed the presence of ceramic contaminations mainly attributed to quartz ($SiO_2$, PDF#79–1910). Furthermore, calcite ($CaCO_3$, PDF#86–2334) and dolomite ($CaMg(CO_3)_2$, PDF#36–04) impurities cannot be excluded. These pollutants prevented the glass powder to be eligible for open-loop recycling route, i.e. remelting.

The volcanic ash diffraction pattern showed various crystalline phase typical of Mt. Etna basaltic rock [38–40]. The significant level of Si and Al, along with Ca, Na, Mg and Fe, contributed to the formation of calcium-rich plagioclase ($Ca_{0.78}Na_{0.22}Al_{1.78}Si_{2.22}O_8$, PDF#89–1480) and other solid solutions, such as iron-containing olivine ($(Mg_{1.215}Fe_{0.785})SiO_4$, PDF#76–0551) and hedenbergite ($Ca_{0.79}Al_{0.06}Fe_{0.08}Mg_{0.47}Fe_{0.6}Si_2O_6$, PDF#74–2425) [41]. Moreover, a huge hump in between 2θ ≈ 20° to 35° confirms the presence of amorphous components into volcanic ash powder [42,43].

The soda-lime glass and volcanic ash-based alkali activated foams exhibited different mineralogical phase compared to starting raw materials. In the sample A, it was evident through the shift of amorphous halo [44] toward higher 2θ (from approximately 25° to 27°) as a consequent formation of amorphous gel as part of secondary phase in mild alkali activation process [17]. Simultaneously, components released in solution were not just involved in the amorphous gel, but there was a rearrangement in crystalline phases. The main peak in alkali activated foams was slightly shifted at higher angles with respect to

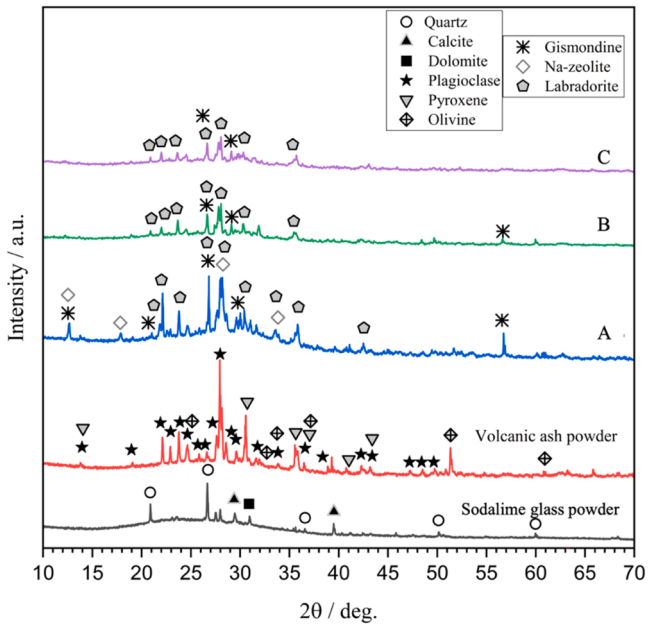


**Fig. 4.** X-ray diffraction analysis of raw materials and samples A, B and C after alkali activation.

plagioclase peak in volcanic ash powder, and it matched satisfactorily with plagioclase (labradorite, $Ca_{0.68}Na_{0.30}(Al_{1.66}Si_{2.34}O_8)$, PDF#83–1372) [45]. Moreover, sodium-zeolite ($Na_8(Al_8Si_8O_{32})(H_2O)_{15.17}$,PDF#89–6322) and calcium-zeolite (gismondine, $CaAl_2Si_2O_8{\cdot}4H_2O$, PDF#20–0452) are detected in the samples A.

The introduction of $Fe_3O_4$@$SiO_2$ nanoparticles have decreased the height of the main peak (2θ ≈ 28°). It was plausible that the formation of zeolite phases formations was inhibited. Indeed, the peaks at of 2θ ≈ 13° associate to Na-zeolite, as well as the peak at 2θ ≈ 57° associated to gismondine are not still detected in samples B and C. The absence of zeolites following the introduction of magnetic nanoparticles has been corroborated by SEM images (Fig. 5c-d).

The addition and the percentage of $Fe_3O_4$@$SiO_2$ nanoparticles have influenced the microstructure of alkali activated foamed materials, as detected by scanning electron microscopy (SEM). In samples that did not contains nanoparticles (Fig. 5a), unreacted volcanic ash and glass powder surrounded by a gel phase could be easily detected. At higher magnification (Fig. 5b) it was highlighted that alkali activation promotes the growth of crystalline zeolites due to the presence of cubic shape typical of these species.

As expected by XRD, zeolites were not still evident after the embedding of $Fe_3O_4$@$SiO_2$ nanoparticles into the slurries. In the sample B, the individual glass and volcanic particles linked together are layered by needle shape potassium carbonates (Figs 5c). Potassium carbonates were not readily evident in the sample contained the highest number of nanoparticles. However, glass and volcanic ash particles appear more glued together, and the highest level of compactness with limited porosity was confirmed by pycnometer measurements detailed in Table S1.

SEM images confirm that secondary-phase in alkali activation of glass is very variable and easily influenced by the starting conditions and initial raw materials. This lead to conclude that the introduction of $Fe_3O_4$@$SiO_2$ prevents the formation of zeolites, and on the other hand promotes the other crystalline phases such as carbonates. Despite zeolites being reducing or missing, samples B and C are eligible for dye sorption as demonstrated in paragraph 3.2.2.

#### 3.2.2. Adsorption and photocatalytic tests

The adsorption capacity of volcanic based materials is a well-known

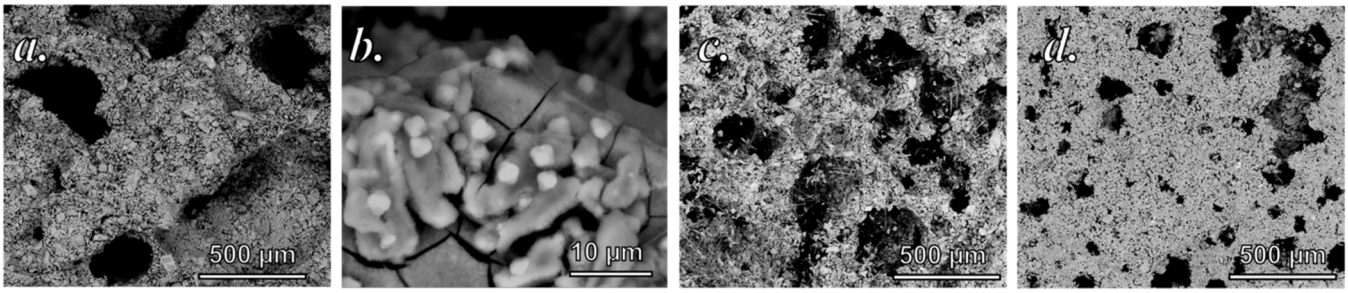


**Fig. 5.** SEM images of samples A (a-b), B (c) and C (d).

phenomenon. Several studies have been reported on this topic demonstrating good sorption efficiency for Cd(II), As(V), Cu(II), Cr(III) and phosphate ions in contaminated water [46–49]. For this reason, and for the low cost and their natural abundance the use of them as adsorbent is in intriguing research topic. In our work, the removal efficiency was evaluated using methylene blue as a model organic pollutant to assess both the adsorption and photocatalytic behaviour of the as-prepared foamed samples (Table 3). The relative removal kinetic curves are reported in Fig. S3, S4 and S5.

Initially, the adsorption capability was evaluated conducted the tests in the dark, to avoid any interferences from the light (Tests 1, 3 and 5). Sample A, prepared without any addition of $Fe_3O_4@SiO_2$, shows a dye removal efficiency of 58 % after 270 min (Test 1,Table 3).

The incorporation of nanoparticles here reported (5 % m/m for Sample B and 10 % m/m for Sample C) led to a modification of the microstructure, as described in the previous paragraph. These concentrations were selected to impart magnetic properties to the final material; excessive amounts were not considered due to possible undesirable effects that will be discussed later. The introduction of the as-prepared nanoparticles was intended to achieve three effects: (i) impart magnetic properties to the foamed samples and increase the removal efficiency of the dye by (ii) enhanced adsorption and (iii) photocatalytic behaviour under visible light. We can observe that:

(i) The composite materials effectively exhibit magnetic properties, offering several advantages - most notably, the ability to be easily and rapidly separated from treated water using an external magnetic field, thereby eliminating the need for filtration or centrifugation in water purification systems.

(ii) Magnetite is a well-known adsorbent material [50–52]. The contribution of magnetite nanoparticles to dye adsorption under dark conditions is clearly demonstrated in Samples B and C. Test 3 (Sample B, 5 % m/m $Fe_3O_4@SiO_2$) and Test 5 (Sample C, 10 % m/m $Fe_3O_4@SiO_2$) showed removal efficiencies of 92 % and 75 %, respectively, both significantly higher than the 58 % observed for Sample A in Test 1 (Fig. 6). Interestingly, increasing the amount of nanoparticles resulted in a decrease in removal efficiency. This behavior is attributed to a progressive reduction in porosity, caused by the occlusion of pores by magnetite nanoparticles - 76.67 % V/V for Sample A, 71.30 % V/V for Sample B, and 68.12 % V/V for Sample C (Table S1). Despite the reduction in porosity, the adsorption efficiencies of both Samples B and C remain higher than that of Sample A, indicating that the contribution of magnetite to dye adsorption outweighs the negative effect of reduced porosity at the selected concentrations.

(iii) Test 2, performed on Sample A under visible light, revealed a higher removal efficiency compared to the dark condition (Test 1), with values of 78 % and 58 %, respectively (Fig. 6). This behaviour can be linked to the sample composition, since the starting materials contains two common photocatalysts, ferric oxide ($Fe_2O_3$) and titanium dioxide ($TiO_2$).

**Table 3**
Summary of dye removal tests conditions.

| Test | Sample | Condition | Removal efficiency ± σ [%] |
|---|---|---|---|
| 1 | A | Dark | 58 ± 4 |
| 2 | A | Visible light | 78 ± 1 |
| 3 | B | Dark | 94 ± 1 |
| 4 | B | Visible light | 96 ± 4 |
| 5 | C | Dark | 75 ± 4 |
| 6 | C | Visible light | 95 ± 0 |

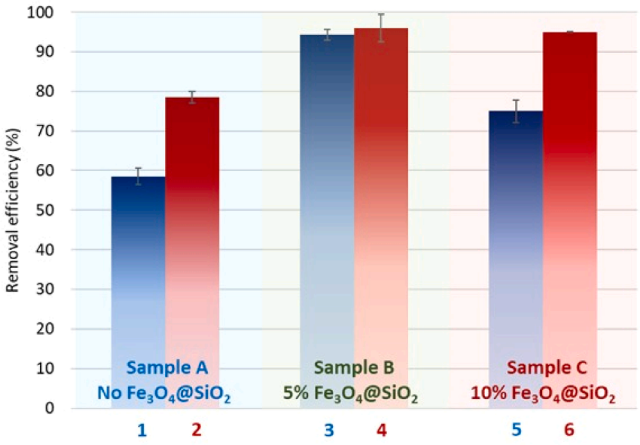


**Fig. 6.** Removal efficiency of the adsorption tests (blue) and of photocatalytic tests (red) in 270 min of the sample A without $Fe_3O_4@SiO_2$ (blue background), sample B with 5 % m/m $Fe_3O_4@SiO_2$ (green background) and sample C with 10 % m/m $Fe_3O_4@SiO_2$ (red background).

Ferric oxide, present in SLG at 0.1 and in VA at 11.9 % m/m, is currently considered a favourable semiconductor for photocatalytic reactions due to its low band gap (2.3 eV) and good harvesting of visible light, excellent stability, recyclability and earth-abundance [27,53].

On the other hand, titanium dioxide, present in both SLG and VA (0.1 % m/m and 1.9 % m/m, respectively; Table 1), is well-known as a photocatalytic material under UV light. However, one of its main limitations in environmental applications is its poor visible-light activity, due to its relatively high band gap (approximately 3.0–3.2 eV) [54]. For this reason, the enhanced photocatalytic activity in our work cannot be attributed to it, since the tests were performed under visible light.

Despite that, in literature various strategies have been explored to reduce the band gap and improve $TiO_2$ photocatalytic activity under visible light. These strategies include doping with non-metallic and transition-metal elements [55,56].

Moreover, literature suggests a doping effect by sulphur and iron that can potentially reduce the band gap and enable light absorption in the visible range. Considering these elements are naturally present in the raw materials, a further photocatalytic contribution could be derived from it [57]. Unfortunately, attempts to determine the band gap values

were unsuccessful. Measurements were carried out on powdered samples using the diffuse reflectance method, applying the Kubelka-Munk function and Tauc plots. However, both direct and indirect transition models failed to exhibit clear linear regions. This issue is likely due to the limitations of the method when the sample does not consist of a single crystalline phase or exhibits significant absorption at low energies [58,59]. As confirmed by XRD analysis, the presence of secondary phases, even in small quantities, can distort the spectra, resulting in blurred absorption edges and ambiguous transitions.

Taking everything into account, we attribute the main photocatalytic effect observed in test 2 to $Fe_2O_3$-enabled photo-Fenton effect [60], while the verification of a possible contribution from doped $TiO_2$ was not confirmed.

Moreover, the introduction of $Fe_3O_4$@$SiO_2$ nanoparticles enhances the photocatalytic activity, thanks to an additional contribution to the photo-Fenton effect promoted by iron [61]. This is clearly evidenced for Sample C, where Test 6 (performed under visible light) yielded a removal efficiency of 95 %, an improvement over both Test 2 (78 %) and Test 5 (75 %). In contrast, for Sample B, this enhancement is less evident, likely because the removal efficiency was already very high in the dark (94 %, Test 3).

Finally, excessive nanoparticle loading was avoided in order to prevent the excessive pore occlusion, within the saturation of active sites, and electron-hole recombination phenomenon [62,63].

## 4. Conclusions

With the aim to remove cationic dye, alkali activated foams were synthesised utilizing volcanic ash and soda-lime glass waste powder. This was supported simply by the addition of safe and affordable foaming and stabilizing agents, such as sodium perborate monohydrate (SPM) and sodium dodecyl sulphate (SDS). Magnetic $Fe_3O_4$ nanoparticles layered by $SiO_2$ are added to the alkali activated slurries to facilitate post-adsorption sample recovery. XRD analyses highlighted that the adsorption properties are not associated to the growing of zeolites in AAFs. The zeolites are not still detected after the embedding of 5 % m/m and 10 % m/m magnetite nanoparticles in samples.

Independent of test conditions (dark or visible light) the samples B, in which 5 % m/m of $Fe_3O_4$@$SiO_2$ nanoparticles are incorporated, turn out to be optimal in terms of removal efficiency, as it maintains an appropriate balance between porosity and the amount of magnetic nanoparticles. Conversely, the addition of higher nanoparticles content leads to the formation of denser samples, less suitable for absorption and photocatalytic application. Nevertheless, future research focuses on evaluating the feasibility of regenerating the foams after the adsorption test. Additional investigation will explore the potential to extend the adsorption and photocatalytic capacity to other dye molecules (i.e. rhodamine).

## CRediT authorship contribution statement

**Francesco Lanero:** Writing – original draft, Visualization, Validation, Investigation, Formal analysis, Data curation. **Giulia Tameni:** Writing – original draft, Visualization, Validation, Investigation, Formal analysis, Data curation. **Eleonora Russo:** Writing – original draft, Investigation, Formal analysis, Data curation. **Paolo Sgarbossa:** Writing – review & editing, Validation, Supervision, Resources, Project administration, Methodology, Conceptualization. **Enrico Bernardo:** Writing – review & editing, Validation, Resources, Project administration, Methodology, Conceptualization.

## Acknowledgements

E.B. and G.T acknowledge Professor Loredana Contrafatto (University of Catania) for providing the volcanic ash. P.S. and F.L. thank the UNIPD-DII BIRD2023 project “HYPURE-Hybrid 3D Printed Water Purification Systems for Emerging Pollutants”, for financial support. E.B and P.S acknowledge the funding from GLASS_Trea.S.U.Res (GLASS-based TREAtments for Sustainable Upcycling of inorganic RESidues) project (PRIN 2022 PNRR project #P2022S4TK2). The authors would like to gratefully thank Dr. Federico Zorzi for experimental assistance with SEM micrographs.

## Supplementary materials

Supplementary material associated with this article can be found, in the online version, at doi:10.1016/j.oceram.2025.100884.

## References

[1] E.O. Alegbe, T.O. Uthman, A review of history, properties, classification, applications and challenges of natural and synthetic dyes, Heliyon. 10 (13) (2024) e33646, https://doi.org/10.1016/j.heliyon.2024.e33646.
[2] A. Xu, Y.H. Wu, Z. Chen, G. Wu, Q. Wu, F. Ling, W.E. Huang, H.Y. Hu, Towards the new era of wastewater treatment of China: development history, current status, and future directions, Water Cycle 1 (2020) 80–87, https://doi.org/10.1016/j.watcyc.2020.06.004.
[3] B.J. Singh, A. Chakraborty, R. Sehgal, A systematic review of industrial wastewater management: evaluating challenges and enablers, JEM 348 (2023) 119230, https://doi.org/10.1016/j.jenvman.2023.119230.
[4] E. Mutegoa, Efficient techniques and practices for wastewater treatment: an update, Discov. Water 4 (2024) 69, https://doi.org/10.1007/s43832-024-00131-8.
[5] K.E. Lee, N. Morad, T.T. Teng, B.T. Poh, Development, characterization and the application of hybrid materials in coagulation/flocculation of wastewater: a review, Chem. Eng. J. 203 (2012) 370–386, https://doi.org/10.1016/j.cej.2012.06.109.
[6] M. Cuccarese, S. Brutti, A. De Bonis, R. Teghil, F. Di Capua, I.M. Mancini, S. Masi, D. Caniani, Sustainable adsorbent material prepared by soft alkaline activation of spent coffee grounds: characterisation and adsorption mechanism of methylene blue from aqueous solutions, Sustainability. 15 (2023) 2454, https://doi.org/10.3390/su15032454.
[7] Y. Ettahiri, L. Bouna, A. Brahim, A. Benlhachemi, B. Bakiz, D. Eliche-quesada, P. Luis, B. Bakiz, J.S. Pedro, Synthesis and characterization of porous and photocatalytic geopolymers based on natural clay: enhanced properties and efficient Rhodamine B decomposition, Appl. Mater. Today 36 (2024) 102048, https://doi.org/10.1016/j.apmt.2023.102048.
[8] H.Y. Ye, H. Xu, C.Z. Wu, J.Z. Guo, Highly efficient removal of organic dyes and heavy metal cation from wastewater by polyphenolate porous coordination polymer, Int. J. Env. Sci. Technol. 20 (2023) 12569–12580, https://doi.org/10.1007/s13762-023-04858-0.
[9] Y. Ettahiri, A. Bouddouch, B. Akhsassi, A. Khali, L. Bouna, A. Benlhachemi, L. Perez-Villarejo, Optimized porous alkali-activated material for superior dye removal: synthesis and performance analysis, Mater. Adv. 7 (2025) 2435–2447, 10.1039.d4ma01065e.
[10] F. Lanero, M. Ramos-Martin, K. Vezzù, V. Di Noto, J. García-Álvarez, A. Scarso, P. Sgarbossa, A.Presa Soto, Cationic fluorinated polyphosphazenes for efficient decontamination of anionic pollutants from wastewater, Macromol. Chem. Phys 226 (2025) e00154, https://doi.org/10.1002/macp.20250015.
[11] A. Haleem, A. Shafiq, S.-Q. Chen, M. Nazar, A comprehensive review on adsorption, photocatalytic and chemical degradation of dyes and nitro-compounds over different kinds of porous and composite materials, Molecules. 28 (3) (2023) 1081, https://doi.org/10.3390/molecules28031081.
[12] T. Luukkonen, A. Heponiemi, H. Runtti, J. Pesonen, J. Yliniemi, U. Lassi, Application of alkali-activated materials for water and wastewater treatment: a review, Rev. Env. Sci. Biotechnol. 18 (2019) 271–297, https://doi.org/10.1007/s11157-019-09494-0.
[13] S.A. Bernal, J.L. Provis, A. Fernandez-Jimenez, P.V. Krivenko, E. Kavalerova, M. Palacios, C. Shi, Binder chemistry- high-calcium alkali-activated materials, in: J. L. Provis, J.S.J. Van Deventer (Eds.), Alkali Activated materials, State-of-the-Art report, RILEM TC 224-AAM, Springer, Dordrecht, 2014, pp. 59–91.
[14] P. Rożek, M. Król, W. Mozgawa, Geopolymer-zeolite composites: a review, J. Clean. Prod. 230 (2019) 557–579, https://doi.org/10.1016/j.jclepro.2019.05.152.
[15] A.R. Romero, N. Toniolo, A.R. Boccacini, E. Bernardo, Glass-ceramic foams from ‘weak alkali activation’ and gel-casting of waste glass/fly ash mixtures, Mater. (Basel) 12 (4) (2019) 588, https://doi.org/10.3390/ma12040588.
[16] D.D. Ramteke, M. Hujova, J. Kraxner, D. Galusek, A.R. Romero, R. Falcone, E. Bernardo, Up-cycling of ‘unrecyclable’ glasses in glass-based foams by weak alkali-activation, gel casting and low-temperature sintering, J. Clean. Prod. 278 (2021) 123985, https://doi.org/10.1016/j.jclepro.2020.123985.
[17] G. Tameni, D. Lago, H. Kaňková, L. Buňová, J. Kraxner, D. Galusek, D.M. Dawson, S.E. Ashbrook, E. Bernardo, Alkaline attack of boro-alumino-silicate glass: new insights of the molecular mechanism of cold consolidation and new applications, Open Ceram. 21 (2025) 100726, https://doi.org/10.1016/j.oceram.2024.100726.
[18] V. Phavongkham, S. Wattanasiriwech, T.-W. Cheng, D. Wattanasiriwec, Effects of surfactant on thermo-mechanical behavior of geopolymer foam paste made with sodium perborate foaming agent, Constr. Build. Mater. 243 (2020) 118282, https://doi.org/10.1016/j.conbuildmat.2020.118282.

[19] L. Korat, V. Ducman, The influence of the stabilizing agent SDS on porosity development in alkali-activated fly-ash based foams, Cem. Concr. Compos. 80 (2017) 168–174, https://doi.org/10.1016/j.cemconcomp.2017.03.010.

[20] M. Cyr, R. Idir, T. Poinot, Properties of inorganic polymer (geopolymer) mortars made of glass cullet, J. Mater. Sci. 47 (2012) 2782–2797, https://doi.org/10.1007/s10853-011-6107-2.

[21] G. Dal Proggetto, P. Douwe, A. Stroscio, E. Kamseu, I. Lancellotti, A. Elimbi, C. Leonelli, Dissolution of volcanic ash in alkaline environment for cold consolidation of inorganic binders, Mater. (Basel) 17 (20) (2024) 5068, https://doi.org/10.3390/ma17205068.

[22] E. Bernardo, H. Elsayed, A. Mazzi, G. Tameni, S. Gazzo, L. Contrafatto, Double-life sustainable construction materials from alkali activation of volcanic ash/discarded glass mixture, Constr. Build. Mater. 359 (2022) 129540, https://doi.org/10.1016/j.conbuildmat.2022.129540.

[23] R.M. Novais, J. Carvalheiras, D.M. Tobaldi, M.P. Seabra, R.C. Pullar, J. A. Labrincha, Synthesis of porous biomass fly ash-based geopolymer spheres for efficient removal of methylene blue from wastewaters, J. Clean. Prod. 207 (2019) 350–362, https://doi.org/10.1016/j.jclepro.2018.09.265.

[24] F. Eshghabadi, V. Javanbakht, Preparation of porous metakaolin-based geopolymer foam as an efficient adsorbent for dye removal from aqueous solution, J. Molec. Struc. 1295 (4) (2023) 136639, https://doi.org/10.1016/j.molstruc.2023.136639.

[25] V. Medri, E. Papa, M. Mor, A. Vaccari, A. Natali Murri, L. Piotte, C. Melandri, E. Landi, Mechanical strength and cationic dye adsorption ability of metakaolin-based geopolymer spheres, Appl. Clay Sci. 193 (2020) 105678, https://doi.org/10.1016/j.clay.2020.105678.

[26] D. Wattanasiriwech, K. Yomthong, S. Wattanasiriwech, Adsorption efficiency and photocatalytic activity of fly ash-based geopolymer foam mortar, Ceram. Int. 47 (19) (2021) 27361–27371, https://doi.org/10.1016/j.ceramint.2021.06.158.

[27] C.N.C. Hitam, A.A. Jalil, A review on exploration of $Fe_2O_3$ photocatalyst towards degradation of dyes and organic contaminants, J. Env. Manag. 258 (2020) 110050, https://doi.org/10.1016/j.jenvman.2019.110050.

[28] M. Kumar, H.S. Dosanjh, J. Singh, K. Monir, H. Singh, Review on magnetic nanoferrites and their composites as alternatives in waste water treatment: synthesis, modifications and applications, Env. Sci. Water Res. Technol. 6 (2020) 491–514, https://doi.org/10.3390/polym16050709.

[29] A. Hojjati-Najafabadi, M. Mansoorianfar, T. Liang, K. Shahin, Y. Wen, A. Bahrami, C. Karaman, N. Zare, H. Karimi-Maleh, Y. Vasseghian, Magnetic-MXene-based nanocomposites for water and wastewater treatment: a review, J. Water Process Eng. 47 (2022) 102696, https://doi.org/10.1016/j.jwpe.2022.102696.

[30] S. Shukla, R. Khan, A. Daverey, Synthesis and characterization of magnetic nanoparticles, and their applications in wastewater treatment: a review, Env. Technol. Innov. 24 (2021) 101924, https://doi.org/10.1016/j.eti.2021.101924.

[31] A. Benli, Sustainable use of waste glass sand and waste glass powder in alkali-activated slag foam concretes: physico-mechanical, thermal insulation and durability characteristics, Constr. Build. Mater. 438 (2024) 137128, https://doi.org/10.1016/j.conbuildmat.2024.137128.

[32] M. Gayathiri, T. Pulingam, K.T. Lee, K. Sudesh, Activated carbon from biomass waste precursors: factors affecting production and adsorption mechanism, Chemosphere 294 (2022) 133764, https://doi.org/10.1016/j.chemosphere.2022.133764.

[33] M. Barozzi, S. Copelli, E. Russo, P. Sgarbossa, M.C. Lavagnolo, A. Sandon, C. Morosini, E. Sieni, Implementation of magnetic nanostructured adsorbents for heavy metals separation from textile wastewater, Sustainability. 14 (18) (2022) 11785, https://doi.org/10.3390/su141811785.

[34] W. Stöber, Arthur Fink, Ernst Bohn, Controlled growth of monodisperse silica spheres in the micron size range, J. Colloid Sci. 26 (1) (1968) 62–69, https://doi.org/10.1016/0021-9797(68)90272-5.

[35] E.S.D.T. de Mendonça, A.C. Britto de Faria, S.C. Loureiro Dias, F.F.H. Aragón, J. C. Mantilla, J.A.H. Coaquira, J.A. Dias, Effects of silica coating on the magnetic properties of magnetite nanoparticles, Surf. Interfaces 14 (2019) 34–43, https://doi.org/10.1016/j.surfin.2018.11.005.

[36] C. Rocchiccioli-Deltcheff, M. Amirouche, Structure and catalytic properties of silica-supported polyoxomolybdates III. 12-molybdosilicic acid catalysts: vibrational study of the dispersion effect and nature of the *Mo species* in interaction with the silica support, J. Catal. 138 (2) (1992) 445–456, https://doi.org/10.1016/0021-9517(92)90296-T.

[37] D. Yang, J. Hu, S. Fu, Controlled synthesis of magnetite-silica nanocomposites via a seeded sol-gel approach, J. Phys. Chem. C (2009) 7646–7652, https://doi.org/10.1021/jp900868d.

[38] R.A. Corsaro, N. Métrich, Chemical heterogeneity of Mt. Etna magmas in the last 15 ka. Inferences on their mantle sources, Lithos. 252-253 (2016) 123–134, https://doi.org/10.1016/j.lithos.2016.02.006.

[39] G. Barone, C. Finocchiaro, I. Lancellotti, C. Leonelli, P. Mazzoleni, C. Sgarlata, A. Stroscio, Potentiality of the use of pyroclastic volcanic residues in the production of Alkali activated material, Waste BioMass Valorization. 12 (2021) 1075–1094, https://doi.org/10.1007/s12649-020-01004-6.

[40] G. Barone, P. Mazzoleni, R.A. Corsaro, P. Costagliola, F. Di Benedetto, E. Ciliberto, D. Gimeno, C. Bongiorno, C. Spinella, Nanoscale surface modification of Mt. Etna volcanic ashes, Geochim, Cosmochim Acta 174 (2016) 70–84, https://doi.org/10.1016/j.gca.2015.11.011.

[41] C. Finocchiaro, G. Barone, P. Mazzoleni, C. Leonelli, A. Gharzouni, S. Rossignol, FT-IR study of early stages of alkali activated materials based on pyroclastic deposits (Mt. Etna, Sicily, Italy) using two different alkaline solutions, Constr, Build, Mater. 262 (2020) 120095, https://doi.org/10.1016/j.conbuildmat.2020.120095.

[42] S. Shoji, S. Kodayashi, I. Yamada, J. Masui, Chemical and mineralogical studies on volcanic ashes I. Chemical composition of volcanic ashes and their classification, Soil Sci, Plant Nutr. 21 (4) (1975) 311–318, https://doi.org/10.1080/00380768.1975.10432646.

[43] S. Zhou, C. Lu, X. Zhu, F. Li, Upcycling of natural volcanic resources for geopolymer: comparative study on synthesis, reaction mechanism and rheological behaviour, Constr, Build, Mater. 268 (2021) 121184, https://doi.org/10.1016/j.conbuildmat.2020.121184.

[44] R. Occhipinti, G. Lanzafame, A. LluverasTenorio, C. Finocchiaro, L. Gigli, M. R. Tinè, P. Mazzoleni, G. Barone, Design of alkali activated foamy binders from Sicilian volcanic precursors, Ceram, Int. 49 (23) (2023) 38835–38846, https://doi.org/10.1016/j.ceramint.2023.09.220. B.

[45] D. Müller, U. Kueppers, K.-U. Hess, W. Song, D.B. Dingwell, Mineralogical and thermal characterization of a volcanic ash: implications for turbine interaction, J. Volcanol, Geotherm. 377 (2019) 43–52, https://doi.org/10.1016/j.jvolgeores.2019.04.005.

[46] P.N. Lemougna, K. Wang, Q. Tang, A.N. Nzeukou, N. Billong, U.C. Melo, C. Xuemin, Review on the use of volcanic ashes for engineering applications, Resour, Conserve, Recycl 137 (2018) 177–190, https://doi.org/10.1016/j.resconrec.2018.05.031.

[47] R. Chen, Z. Zhang, Y. Yang, Z. Lei, N. Chen, X. Guo, C. Zhao, N. Sugiura, Use of ferric-impregnated volcanic ash for arsenate (V) adsorption from contaminated water with various mineralization degrees, J. Colloid, Interface Sci. 353 (2) (2011) 542–548, https://doi.org/10.1016/j.jcis.2010.09.066.

[48] J.Y. Kim, M.S. Balathanigaimani, H. Moon, Adsorptive removal of nitrate and phosphate using MCM-48, SBA-15, Chitosan, and volcanic pumice, Water. Air. Soil. Pollut. 226 (2015) 431, https://doi.org/10.1007/s11270-015-2692-z.

[49] M. Yavuz, F. Gode, E. Pehlivan, S. Ozmert, Y.C. Sharma, An economic removal of $Cu^{2+}$ and $Cr^{3+}$ on the new adsorbents: pumice and polyacrylonitrile/pumice composite, Chem, Eng, J. 137 (3) (2008) 453–461, https://doi.org/10.1016/j.cej.2007.04.030.

[50] T. Tuutijärvi, J. Lu, M. Sillanpää, G. Chen, As(V) adsorption on maghemite nanoparticles, J. Hazard, Mater. 166 (2–3) (2009) 1415–1420, https://doi.org/10.1016/j.jhazmat.2008.12.069.

[51] F. Raganati, M. Alfe, V. Gargiulo, R. Chirone, P. Ammendola, Kinetic study and breakthrough analysis of the hybrid physical/chemical $CO_2$ adsorption/desorption behavior of a magnetite-based sorbent, Chem, Eng, J. 372 (2019) 526–535, https://doi.org/10.1016/j.cej.2019.04.165.

[52] X.S. Wang, L. Zhu, H.J. Lu, Surface chemical properties and adsorption of Cu (II) on nanoscale magnetite in aqueous solutions, Desalination. 276 (1–3) (2011) 154–160, https://doi.org/10.1016/j.desal.2011.03.040.

[53] M. Mishra, D-M. Chun, α-Fe2O3 as a photocatalytic material: a review, Appl. Catal. 498 (2015) 126–141, https://doi.org/10.1016/j.apcata.2015.03.023.

[54] Z. Kovačič, B. Likozar, M. Huš, Electronic properties of rutile and anatase $TiO_2$ and their effect on $CO_2$ adsorption: a comparison of first principle approaches, Fuel 328 (2022) 125322, https://doi.org/10.1016/j.fuel.2022.125322.

[55] A. Khlyustova, N. Sirotkin, T. Kusova, A. Kraev, V. Titov, A. Agafonov, Doped $TiO_2$: the effect of doping elements on photocatalytic activity, Mater, Adv. 1 (2020) 1193–1201, https://doi.org/10.1039/D0MA00171F.

[56] G.E. Orizu, P.E. Ugwuoke, P.U. Asogwa, S.U. Offiah, A review on the inference of doping $TiO_2$ with metals/non-metals to improve its photocatalytic activities, IOP Conf. Ser. Earth Environ. Sci. 1178 (1) (2023) 012008, https://doi.org/10.1088/1755-1315/1178/1/012008.

[57] D. Rosa, N. Abbasova, L. Di Palma, Titanium dioxide nanoparticles doped with iron for water treatment via photocatalysis: a review, Nanomaterials 14 (3) (2024) 293, https://doi.org/10.3390/nano14030293.

[58] H. Heryanto, D. Tahir, Composite fayalite with 5 % laterite soil and iron sand: structural properties and band gap calculation based on theoretical Kubelka-munk, Taylor expansion, and self-consistent field method, JOM 75 (2023) 5264–5272, https://doi.org/10.1007/s11837-023-05828-0.

[59] P. Makula, M. Pacia, W. Macyk, How to correctly determine the band gap energy of modified semiconductor photocatalysts based on UV–Vis spectra, J. Phys. Chem. Lett 9 (23) (2018) 6814–6817, https://doi.org/10.1021/acs.jpclett.8b02892.

[60] A. Boudjemaa, A. Rebahi, B. Terfassa, R. Chebout, T. Mokrani, K. Bachari, N. J. Coville, Fe2O3/carbon spheres for efficient photo-catalytic hydrogen production from water and under visible light irradiation, Sol. Energy Mater. Sol. Cells 140 (2015) 405–411, https://doi.org/10.1016/j.solmat.2015.04.036.

[61] M. Minella, G. Marchetti, E. De Laurentiis, M. Malandrino, V. Maurino, C. Minero, D. Vione, K. Hanna, Photo-Fenton oxidation of phenol with magnetite as iron source, Appl. Catal. B: Environ. 154-155 (2014) 102–109, https://doi.org/10.1016/j.apcatb.2014.02.006.

[62] X. Chen, S.S. Mao, Titanium dioxide nanomaterials: synthesis, properties, modifications, and applications, Chem. Rev. 107 (2007), https://doi.org/10.1021/cr0500535, 2891-295.

[63] Q. Wang, K. Domen, Particulate photocatalysts for light-driven water splitting: mechanisms, challenges, and design strategies, Chem. Rev. 120 (2) (2020) 919–985, https://doi.org/10.1021/acs.chemrev.9b00201.